

pubs.acs.org/JPCC Article

# Examining the Effect of Dopant Ionic Radius on Plasmonic M:ZnO Nanocrystals ( $M = Al^{3+}$ , $Ga^{3+}$ , $In^{3+}$ )

Carl R. Conti, III, James R. McBride, and Geoffrey F. Strouse\*



Cite This: J. Phys. Chem. C 2021, 125, 7772–7779



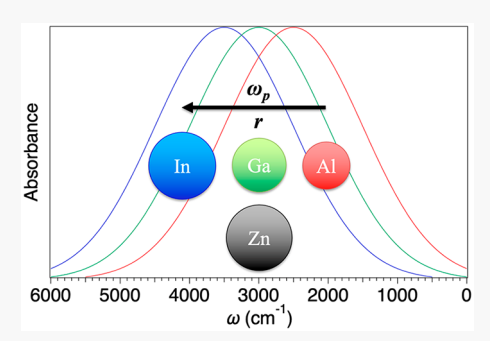
**ACCESS** 

Metrics & More

Article Recommendations

Supporting Information

ABSTRACT: Understanding the role of dopant deactivation on plasmon frequency and extinction is important for the rational design of plasmonic semiconductor nanocrystals (PSNCs). Aliovalent dopants do not always contribute a free carrier to a localized surface plasmon resonance (LSPR) for many reasons, including the existence of a depletion region, the pinning of carriers at neutral defect sites, or even the formation of a secondary insulating microphase (inclusions) not observable in the powder X-ray diffraction (pXRD). Here, we investigate such possibilities and their role in determining the LSPR frequency of Al-, Ga-, and In-doped ZnO NCs. Elemental analysis, pXRD, and absorption measurements are utilized to examine the impact of dopant incorporation on the resulting properties. Both simple and advanced effective mass Drude models are used to fit the mid-infrared plasmons, while one-electron oxidant chemical titrations are used as an independent measure of



the free electron concentrations. The results of these analyses indicate that dopant/host lattice mismatch leads to inefficient carrier generation for aliovalent substitution, potentially due to local spinel-like inclusions. Smaller dopant ions are more likely to incorporate interstitially and form spinel phases, which results in an increased number of pinned carriers. Improved size matching from Al<sup>3+</sup> to In<sup>3+</sup> results in increased substitution efficiency and subsequently higher free carrier concentrations and LSPR frequencies. Drude model correction factors are calculated for each sample and compared to the literature value for *n*-ZnO determined via full band structure calculations. Each dopant is shown to have a unique correction factor, further illustrating the effect of differing ionic radii on the resulting LSPR.

# **■ INTRODUCTION**

Plasmonic semiconductor nanocrystals (PSNCs) have become an increasingly important area of research due to their advantages over traditional metallic plasmonic systems that include tunable carrier density via doping, complete transparency in the visible region, and their ability to strongly absorb near and mid-infrared (NIR, MIR) wavelengths. These unique properties have led to applications in the fields of sensing, decreased electrochromics, and catalysis. For a typical plasmonic system, the plasma frequency ( $\omega_p$ ) is primarily determined by the total number of free carriers (n) and the effective mass ( $m^*$ ) of these carriers, as illustrated by the Drude-Lorentz model,

$$\omega_p = \sqrt{\frac{ne^2}{m^* \varepsilon_0}} \tag{1}$$

where e is the elementary charge of the free carrier and  $\varepsilon_0$  is the permittivity of free space. <sup>13</sup> For systems with the same concentration of aliovalent dopant ion, it is expected that the same number of free carriers would be generated. However, it has been shown in recent literature that as the dopant atom for ZnO changes down group III (Al<sup>3+</sup> to In<sup>3+</sup>),  $\omega_p$  shifts to higher frequencies. <sup>14,15</sup> The origin of this phenomenon has not yet been thoroughly investigated, but this observation could be

explained in two ways: (1) an increase in carrier density as the dopant changes from  $AI^{3+}$  to  $In^{3+}$  or (2) a decrease in the value of  $m^*$ . The change in the ionic radius of the dopant atom can lead to better size matching with  $Zn^{2+}$  and increased dopant activation (i.e., higher values of n). However, better size matching of the dopant and host lattice ions could result in increased carrier mobility and therefore a decrease in  $m^*$ .

While much of the PSNC research has focused on ITO,  $^{16-20}$  studies on Al:ZnO reveal plasmonic behavior that is size, dopant, and reaction dependent.  $^{14,21,22}$  n-type ZnO is an industrially important material, as it has long been studied as a less expensive alternative to indium tin oxide (ITO) for transparent conducting oxide applications.  $^{23-25}$  M:ZnO nanocrystals (MZO NCs, where  $M = Al^{3+}$ ,  $Ga^{3+}$ , or  $In^{3+}$ ) exhibit a localized surface plasmon resonance (LSPR) in the MIR region.  $^{14,21}$  Such low frequency LSPRs make these materials important for applications such as surface-enhanced

Received: January 20, 2021 Revised: March 16, 2021 Published: April 1, 2021





Raman<sup>26,27</sup> and thermal waste management.<sup>28,29</sup> The method developed by Hutchison and co-workers<sup>30</sup> for the controllable synthesis of metal oxide PSNCs was modified by Gaspera and co-workers for ZnO based systems, allowing for a broader study of the group III dopant effects on the LSPR in ZnOs.<sup>15</sup>

In this manuscript, the influence of group III doping on the frequency, extinction, and line width of LSPRs are investigated for spherical, oleic acid passivated AZO, GZO, and IZO NCs using a combination of analytical methods. The effect of dopant incorporation on the crystal structure is investigated via Vegard analysis of powder X-ray data and correlated to the change in the observed LSPR. The simple and advanced effective mass Drude models are utilized to evaluate the measured MIR LSPR, while a one-electron oxidant chemical titration method is used as a direct measure of the total number of carriers for each sample. Utilizing this independent measurement of free carrier concentration allows for the Drude correction factor to be calculated for each sample, and these values are compared to that obtained via full band structure calculations of n-ZnO. These results serve to highlight the importance of dopant activation and the various mechanisms through which deactivation occurs in plasmonic semiconductor NCs, which is critical toward the future rational design of these materials.

# MATERIALS AND METHODS

Indium(III) acetate (In(OAc)<sub>3</sub>, 99.99%), aluminum(III) acetylacetonate (Al(acac)<sub>3</sub>, 99.99%), oleic acid (90%, technical grade), 1,2,4,5-tetrafluorobenzene (C<sub>6</sub>H<sub>2</sub>F<sub>4</sub>, 99%) and tetrachloroethylene (spectrophotometric grade, 99+%) were purchased from Alfa Aesar (Ward Hill, MA). Oleyl alcohol (80-85%, technical grade), gallium(III) acetylacetonate (Ga- $(acac)_3$ ,  $\geq 99.99\%$ ) and nitrosonium tetrafluoroborate (NOBF<sub>4</sub>) were purchased from Beantown Chemical (Hudson, NH). Acetone ( $\geq$ 99.5%), ethanol (95%), acetonitrile  $(\geq 99.9\%, \text{ anhydrous})$ , and nitric acid (67-70%, for trace)metal analysis) were purchased from VWR (Suwanee, GA). Toluene (>99.5%), oleylamine (70%), and zinc(II) acetate dihydrate ( $Zn(OAc)_2 \cdot 2H_2O_2 \ge 98\%$ ) were purchased from Sigma-Aldrich (St. Louis, MO). Tetrachloroethylene was stored with 3 Å molecular sieves. All other chemicals were used as received.

**Synthesis of MZO Nanocrystals.** MZO NCs were synthesized using a modified method previously reported by Gaspera and co-workers. MIS X mmol of  $Al(acac)_3$ ,  $Ga(acac)_3$ , or  $In(OAc)_3$  were combined with 1-X mmol of  $Zn(OAc)_2$  dihydrate and 2 mL of oleic acid. This mixture was degassed at 110 °C for 1 h, followed by the addition of 1 mL of oleylamine and subsequent degassing for 10 min. The metal oleate precursors are then added dropwise at a rate of 0.3 mL/min to 12.5 mL of oleyl alcohol kept at 240 °C while  $N_2$  was continuously run over the reaction. After the injection was complete, the solution was kept at 240 °C for an additional 20 min, followed by cooling to room temperature (rt) and isolation/cleanup of the NCs using toluene/ethanol (3×) and centrifugation.

**Elemental Analysis.** Inductively coupled plasma-mass spectrometry (ICP-MS) was performed using a Thermo Scientific iCAP RQ ICP-MS to confirm the ratio of (Al, Ga, In)/Zn in the NCs. Samples were digested in concentrated nitric acid and then diluted to 2% HNO<sub>3</sub>. Calibration curves were prepared from serial dilutions of an Al/Ga/In/Zn standard dissolved in 2% nitric acid with  $R^2$  values greater

than 0.995 for all ions. Each sample was measured in triplicate after an initial survey run, and there was a minimum of 30 s wash time between samples.

**Powder X-ray Diffraction (pXRD).** pXRD patterns were collected with a Rigaku MiniFlex powder X-ray diffractometer using a Cu–K $\alpha$  source. Samples were dried out, crushed into a fine powder, and then loaded onto a zero-background micropowder plate. Scans were collected from 20 to 70°  $2\theta$  at a rate of 5°/min and a 0.1° step size. Whole powder pattern fitting and the Halder-Wagner method for Scherrer analysis were completed using the Rigaku SmartLab Studio software and performed for all NCs.

Transmission Electron Microscopy (TEM). Nanocrystal samples were diluted and suspended in hexanes and then drop-cast onto Formvar-coated copper TEM grids (Ted Pella) and allowed to dry in a desiccator overnight. Experiments were performed at the Vanderbilt Institute of Nanoscale Science and Engineering using a FEI Tecnai Osiris electron microscope operating at 200 kV.

**UV-Visible-NIR Spectroscopy.** Purified MZO NCs were suspended in tetrachloroethylene and diluted to appropriate concentrations. UV-vis-NIR data was collected using a PerkinElmer Lambda 950 spectrophotometer. A 1 cm path length NIR Quartz cuvette from Spectrocell was used for all absorption experiments. Spectra were baseline corrected using neat tetrachloroethylene and normalized to the band edge absorption of the NCs.

Fourier-Transform Infrared Spectroscopy (FTIR). Purified MZO NCs were suspended in tetrachloroethylene and diluted to appropriate concentrations. Samples were then loaded into a Pike Technologies Liquid FTIR cell with BaF<sub>2</sub> windows and a path length of 0.5 mm. FTIR measurements were performed in transmission mode using a Jasco 6800 FTIR spectrometer. Ligand absorption features were removed using Jasco's Spectra Manager software and the spectra were smoothed using a Savitzky—Golay filter.

NOBF<sub>4</sub> Titrations. The one electron oxidation of the NCs was adapted from ref 58. A known concentration of purified MZO NCs was suspended in dry tetrachloroethylene and brought into an inert atmosphere glovebox. A known concentration of NOBF4 in MeCN was titrated into the NC suspension and left to oxidize for 30 min. After this time, the LSPR was measured via transmission FTIR (described above) and then the liquid cell was returned to the glovebox. This procedure was repeated until the LSPR absorbance did not decrease upon oxidation. The absorbance at each titration point was integrated in order to account for changes in the shape of the LSPR. The linear region of the titration was then extrapolated to determine the amount of NOBF<sub>4</sub> theoretically required to completely extract all free carriers. This number was then converted to the carrier density of the NCs by dividing the extracted number of electrons by the volume of NCs in the suspension calculated using the density of zinc oxide and the size of the NCs.

**Solution NMR Spectroscopy.** Solution <sup>19</sup>F NMR was performed using a 400 MHz Bruker AVIII spectrometer. The concentration of the NOBF<sub>4</sub> in MeCN solution was determined using a known concentration of 1,2,4,5-tetrafluor-obenzene as an internal standard and by measuring the ratio of the integrated NOBF<sub>4</sub> feature to the tetrafluorobenzene signal, following the procedure in ref 58. (Supporting Information).

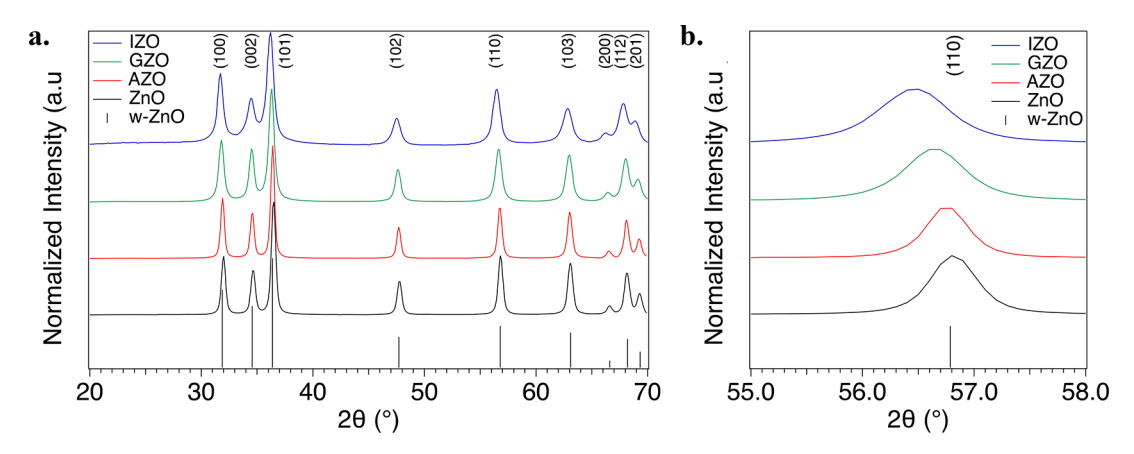


Figure 1. (a) pXRD of ZnO and MZO NCs indexed to the wurtzite ZnO card (PDF #036-1451) and (b) closeup of the (110) lattice reflection for each sample. This feature shifts ~0.3° down with increasing size of the dopant ion.

#### RESULTS AND DISCUSSION

ZnO and MZO (M = Al³+, Ga³+, or In³+) NCs were synthesized following the procedure of Gaspera and coworkers. The MZO samples are ~10 nm in size and exhibit electron diffraction patterns assignable to a hexagonal lattice. (Supporting Figures S1–S3). The M:Zn incorporation into the MZO samples is 12%, as verified by inductively coupled plasma-mass spectrometry (ICP-MS). Powder X-ray diffraction (pXRD) patterns (Figure 1a) are assigned to the hexagonal wurtzite phase of ZnO (PDF #036-1451) and the sizes extracted by fitting the patterns via Scherrer analysis using whole powder pattern analysis corroborates the 10 nm size measured in TEM. All analytical data for the MZO samples are available in the Supporting Information.

The incorporation of the aliovalent Al<sup>3+</sup>, Ga<sup>3+</sup>, or In<sup>3+</sup> guest ion into the ZnO host lattice, whether as a substitutional ion or an interstitial dopant, can either produce a n-type free carrier or introduce Zn vacancies (V<sub>Zn</sub>) to ensure charge balance is maintained.<sup>31</sup> The effect on the pXRD pattern's average lattice spacing is telling, as a substitutional ion without vacancy formation is expected to follow Vegard's law reflecting the cation size difference, while V<sub>Zn</sub> or interstitial ion occupation would likely deviate from the predicted Vegard law behavior. As smaller dopant atoms substitute at Zn host sites, the dspacing in the lattice is expected to decrease and diffraction peaks will move to higher values of  $2\theta$  following Bragg's law.<sup>32</sup> The difference in size for substitutional occupation of the fourcoordinate Zn site by Al<sup>3+</sup> (0.53 Å), Ga<sup>3+</sup> (0.61 Å), and In<sup>3+</sup> (0.76 Å) dopant ions relative to  $\text{Zn}^{2+}$   $(0.74 \text{ Å})^{33}$  suggests that a clear increasing trend in d-spacing should be observable if all aliovalent ions occupy Zn sites.

The (110) reflection in the pXRD patterns (Figure 1b, Supporting Figure S4) is seen to shift to lower values of  $2\theta$  or larger d-spacing with  $M^{3+}$  incorporation. From the Vegard behavior prediction for a substitutional site occupation,  $^{3+}$  the shift to lower  $2\theta$  is expected for  $In^{3+}$  as it is a slightly larger ion than  $Zn^{2+}$ , but not for the smaller  $Al^{3+}$  and  $Ga^{3+}$  ions. This phenomenon has previously been observed for group III-doped ZnO. Occupation of an interstitial site rather than the substitutional site could result in the observed d-spacing shift for the smaller cation. As cations are introduced into interstitial sites, the lattice will slightly expand to accommodate them, provided the atom is not significantly smaller than the interstitial space in which it occupies. As such, the pXRD shift for  $Al^{3+}$  and  $Ga^{3+}$  indicates that a significant percentage of

these dopants may lie interstitially compared to In<sup>3+</sup>, which typically incorporates substitutionally due to the excellent size matching. As a note, the larger GZO shift relative to AZO is believed to be due to the larger size of the Ga<sup>3+</sup> ion, not less efficient substitution. This conclusion is supported by the expected Vegard behavior for each dopant given their relative size mismatches as well as the higher LSPR frequency of GZO compared to AZO.

The free carrier properties in the MZO samples can be evaluated by analysis of the LSPR via the Drude-Lorentz model<sup>13</sup> and from the band edge shift using Tauc plots.<sup>36</sup> The UV-vis-NIR absorption spectra for ZnO and MZO NCs suspended in tetrachloroethylene is shown in Supporting Figure S5. As expected, the NCs are primarily transparent across the visible region and show a sharp increase in absorbance past 400 nm that is assigned to the band edge. The first derivative of the normalized absorption data is shown in the inset of Supporting Figure S5, allowing assignment of the  $1S-1S_{3/2}$  exciton transition at 375 nm (3.30 eV) for the undoped ZnO, consistent with literature reports.<sup>37</sup> As dopant ions are incorporated into the lattice, the exciton peak broadens and undergoes a hypsochromic shift to 3.36 eV. A direct band gap Tauc plot of this data reveals shifts in the optical  $E_g$  (3.26-3.29 eV), but no definitive correlation to ionic radii is observed (Supporting Figure S6). The change in band intensity is believed to reflect changes to the band structure from dopant incorporation, either via the breaking of symmetry or due to the presence of donor-acceptor states.<sup>3</sup>

The LSPR absorption feature provides more information about the effects of the different sized dopants on the resulting carrier density. In Figure 2, the observed LSPR extinction spectra are shown for AZO, GZO, and IZO. The spectra are fit using the Drude-Lorentz model<sup>13</sup> assuming a constant value of  $m^*$  (n-ZnO, 0.23 $m_e$ )<sup>38</sup> and using an average value of 3.11 for the high frequency dielectric constant.<sup>39</sup> The extracted values of  $\omega_m$   $\Gamma$ , and n are listed in Table 1. A linear increase in carrier density with the ionic radius of the dopant atom is observed. While the observed shift in the LSPR parameters could be accounted for by a combination of empirical arguments including carrier delocalization via enhanced orbital expansion and changes to ionization potential as one progresses down a periodic group, such perturbations should also be reflected in the value of  $m^*$ . Therefore, it is critical to directly extract the value of carriers via chemical titration in order to accurately evaluate the changes in the extracted Drude parameters for

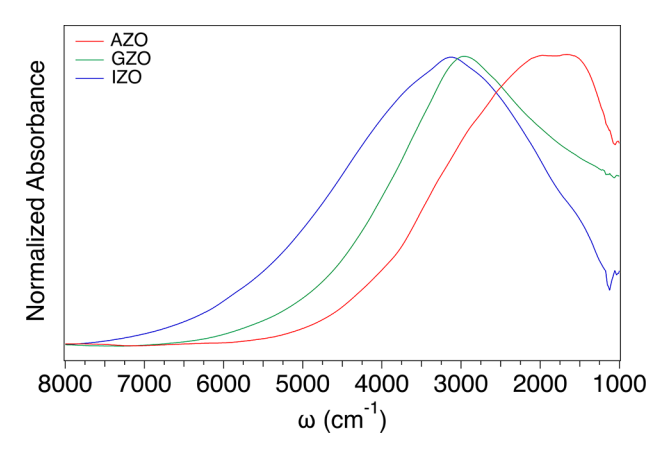


**Figure 2.** FTIR spectra of MZO NCs. Surface ligand absorption features have been removed for clarity.

Table 1. Simple Drude Model Fitting of AZO, GZO, and IZO NCs<sup>a</sup>

	AZO	GZO	IZO
Drude-Lorentz Fitting			
$\omega_p \; (\mathrm{cm}^{-1})$	$4940 \pm 10$	$6580 \pm 20$	$8010 \pm 10$
$\Gamma$ (cm <sup>-1</sup> )	$1915 \pm 8$	$2380 \pm 15$	$2590 \pm 10$
$n/10^{20} \text{ (cm}^{-3}\text{)}$	$0.654 \pm 0.002$	$1.159 \pm 0.004$	$1.716 \pm 0.002$
e <sup>-</sup> /dopant	$0.081 \pm 0.001$	$0.143 \pm 0.001$	$0.212 \pm 0.001$
NOBF <sub>4</sub> Titration			
$n/10^{20} \text{ (cm}^{-3}\text{)}$	$12.3 \pm 0.3$	$13.4 \pm 0.3$	$15.4 \pm 0.4$
e <sup>-</sup> /dopant	$1.53 \pm 0.04$	$1.66 \pm 0.04$	$1.91 \pm 0.05$

<sup>&</sup>lt;sup>a</sup>Data were fit using MATLAB code from ref 13. NOBF<sub>4</sub> titration was adapted from ref 58.

each LSPR, since fitting the data using the simple Drude model assumes a constant  $m^*$  for all samples.

In Table 1, a comparison is made between the Drude extracted carrier densities and the chemical titration measured carrier densities determined by observing the change in LSPR as the MZO sample is titrated against the one electron oxidant (NOBF<sub>4</sub>) (Supporting Figure S8). An increase in carrier density from Al3+ to In3+ is observed; however, the extracted carrier densities are approximately an order of magnitude higher than those predicted by the Drude model. Plotting the Drude and NOBF<sub>4</sub> measured carrier densities for each sample as a function of dopant size mismatch reveals a linear trend (Figure 3). As the size mismatch increases from In<sup>3+</sup> to Al<sup>3+</sup>, the carrier density continues to decrease. The lack of free carriers generated per dopant ion is referred to as dopant deactivation and is an important property to consider when examining PSNCs, as high levels of deactivation can significantly affect the resulting plasmonic properties. 40,41

One plausible explanation for the observed cation size dependence has been previously suggested in the AZO thin film literature. The large size mismatch of  $Al^{3+}/Zn^{2+}$  results in poor dopant solubility at higher concentrations, which induces a conductivity limit in thin films, past which adding more  $Al^{3+}$  dopant does not induce more  $Al^{4}_{Zn}$  defects to form. Instead, the dopant ions begin to form insulating layers of  $Al_2O_3$  at the grain boundaries of the thin film. This phenomenon should hold true for  $Ga^{3+}$  and  $In^{3+}$  as well, but the increasing dopant solubility of these ions due to better size matching will lead to a higher percent of  $M^{4}_{Zn}$  defects forming for these larger dopant ions. Hard X-ray photoelectron spectroscopy (XPS)

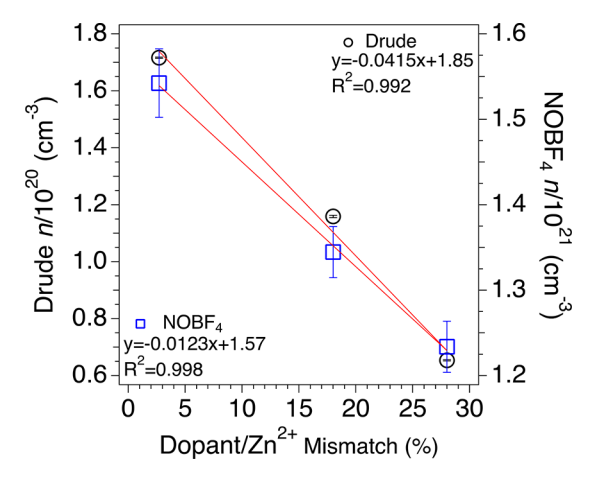


**Figure 3.** Drude and NOBF<sub>4</sub> measured carrier densities vs relative size mismatch of the incorporated dopant with respect to the Zn host site.

studies by Gabás et al. have even suggested that Ga incorporates only as a substitutional dopant in ZnO films. This is applicable to PSNCs in that only a certain percentage of the nominal dopant concentration will aliovalently substitute and generate a free carrier for the LSPR. The Kröger-Vink notation for this aliovalent substitution defect is shown in eq

$$(2M'_{Zn}:O''_i)^x \to 2M'_{Zn} + \frac{1}{2}O_2(g) + 2e'$$
 (2)

$$4M_2O_3 + 3Zn_{Zn}^x \rightarrow (2M_{Zn}^2:V_{Zn}^{"})^x + 3ZnM_2O_4$$
 (3)

Free charge carriers can also be generated via the interstitial incorporation of dopant ions, but this inclusion at the octahedral interstitial sites of w-ZnO will favor the formation of insulating spinel (AB<sub>2</sub>X<sub>4</sub>) inclusions (eq 3) within the PSNC. Evidence for the formation of spinel inclusions in Cr:ZnSe NCs has been previously reported by the Strouse group  $^{46}$  and the ZnAl<sub>2</sub>O<sub>4</sub>/ZnGa<sub>2</sub>O<sub>4</sub> spinels are known to form more readily than the ZnIn<sub>2</sub>O<sub>4</sub> analogue due to the smaller size of the B site cation.  $^{47}$ 

The absolute values for the number of free carriers generated per dopant atom can be calculated for each carrier density value by using the measured values for the size of the NCs and the ICP-MS confirmed dopant concentrations (Table 1). The difference in NOBF<sub>4</sub> measured carrier densities, when compared to Drude model calculated values, provides a measure of the dopant deactivation for each MZO sample. Since carrier density increases and the dopant concentration remains constant, the number of free carriers/dopant follow the same inverse trend with relative size mismatch. The values tabulated using the Drude model carrier densities indicate very low dopant activation of roughly 8 to 21%. This explains why the LSPRs of MZO NCs appear at very low frequencies when compared to other PSNCs such as ITO,<sup>41</sup> despite ITO having a larger value for  $m^*$ .<sup>48</sup>

The deactivated dopants can be accounted for in a number of ways. The first of these is the formation of an insulating spinel phase, as previously discussed. The next likely source of deactivation lies in the existence of a surface depletion region, where dangling bonds at the surface result in pinned carriers that do not contribute to the resulting LSPR feature. Using the parameters needed to calculate the width of the surface depletion region at a given carrier density for ZnO, a 0.7 nm

depletion width is expected for a free carrier density of 1 × 10<sup>21</sup> cm<sup>-3</sup> (approximated from the NOBF<sub>4</sub> measured values). For a spherical, 10 nm NC, this 0.7 nm surface depletion region would result in ~20% dopant deactivation, provided the dopant is incorporated homogeneously as is the case for the bottom-up slow injection synthetic method utilized in this study. 15,30 Detailed calculations and equations used to determine the percentage of deactivated NC are included in the Supporting Information. Studies by Hutchison and coworkers suggest that surface passivation by a nondoped metal oxide layer enhances plasmonic properties, signifying that surface depletion is a contributor. 51 Since the NOBF<sub>4</sub> measured free carrier densities are about 10× greater than those determined via the Drude model, the existence of a surface depletion region can only account for roughly 20% of dopant deactivation in the MZO NCs.

A third source of dopant deactivation lies in the pinning of carriers at anion vacancies within the crystal, which would produce F-centers. These defects are well-known in ZnO<sup>52,53</sup> and result in the introduction of color to an otherwise transparent semiconductor. Each plasmonic sample exhibits a unique color depending on the dopant (Supporting Figure S9), which supports the formation of F-centers in these samples. Oxygen vacancies that are generated both intrinsically and/or as a side effect of aliovalent substitution can pin free carriers in anionic sites where they will not contribute to the observed LSPR. However, these F-centers can still be titrated via NOBF4, which would result in inflated values for the free carrier density measurements. This is also shown in Table 1, where the NOBF<sub>4</sub> determined free carriers/dopant all exceed values of 1, the theoretical maximum for aliovalent substitution efficiency. These results suggest that there are a number of defect sites being generated upon dopant incorporation that result in "invisible carriers", in that they do not contribute to the LSPR and therefore its frequency/extinction. It is also shown in Figure 3 that the slope of the Drude fit is ~3.4× greater than that of the chemical titration fit. Since the Drude model only accounts for carriers that contribute to the observed LSPR, while the chemical titration totals all free electrons (including those trapped at defect sites), this suggests that there are more pinned carriers than free carriers. The greater number of pinned carriers formed compared to free carriers generated via aliovalent substitution means that the increase in free electron count shown in the Drude model has a small effect on the total electron concentration and therefore results in a lower value for the slope of the NOBF<sub>4</sub> plot.

The presence of lattice effects on carrier deactivation leading to spectral changes in the LSPR is also evidenced in the LSPR dampening value ( $\Gamma$ ). This is not surprising, as the dampening term is typically dictated by surface, impurity, electron–electron (el-el), and electron–phonon (el-ph) based scattering mechanisms. Since each sample has a similar size, morphology, and concentration of dopant ions, the effects from surface and impurity scattering can be considered to be negligible across the MZO NCs. An increase in carrier density would result in higher el-el scattering and therefore an increase in  $\Gamma$ . The Drude fitting reflects this trend as  $\Gamma$  increases linearly with carrier density from Al<sup>3+</sup> to In<sup>3+</sup> (Supporting Figure S10). This trend supports the hypothesis that IZO NCs generate a larger number of free carriers due to the better size match of In<sup>3+</sup>/Zn<sup>2+</sup> compared to that of Al<sup>3+</sup> and Ga<sup>3+</sup>.

While higher dopant activation can account for the increases in both  $\omega_{\nu}$  and  $\Gamma$ , the NOBF<sub>4</sub> measured carrier densities are

still approximately 1 order of magnitude higher than those determined using the simple Drude model. One method for examining the effects of these additional electrons is to compare to the literature value for a corrected Drude model previously proposed by Jung and Pederson for ZnO. This model examines the large deviations between the calculated and experimentally measured  $\omega_p$  by using a simple effective mass approach compared to using full band structure calculations specifically for ZnO. The proposed advanced effective mass model of  $\omega_p$  contains a correction term to eq 1 in order to account for this deviation.

$$\omega_p^2 = \frac{e^2 n}{\varepsilon_0 m^*} \frac{1}{\sqrt{1 + (9\pi^2 n)^{2/3} \hbar^2 / (m^* \alpha)}}$$
(4)

In this equation,  $\alpha$  is the correction factor designed to account for the change in local band shape as the Fermi level moves further into the conduction band with increased n-type doping. The change in the degree of parabolicity of the local density of states (LDOS) results in a deviation in the value of  $m^*$ , a phenomenon that has been previously shown in plasmonic ITO and InN NCs. In other words,  $m^*$  cannot always be treated as a constant with increasing values of n and a varying Fermi level relative to the conduction band minimum. This holds doubly true for MZO systems, for which the change in dopant identity and site incorporation will also change the aliovalent substitution efficiency within for each sample.

By combining the experimentally measured values of  $\omega_p$  (obtained via FTIR) and n (obtained via chemical titration), the value for  $\alpha$  can be calculated and the relationship between n and  $\omega_p$  can be modeled for each sample. These values, and their effect on the deviation from the simple Drude model, are presented in Figure 4. The degree to which each sample varies

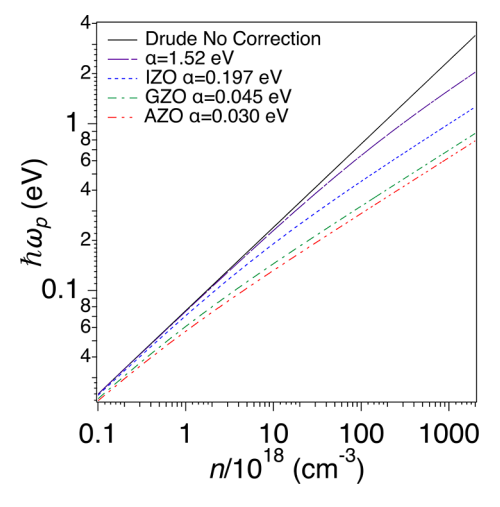


**Figure 4.** Advanced effective mass model calculations for MZO NCs compared to the uncorrected Drude model and the literature value for ZnO  $\alpha = 1.52 \text{ eV}^{49}$ .

from the simple Drude model calculated values corresponds to the ionic radius of the dopant. The uncorrected Drude model is linear on a log/log scale, while the MZO samples start similarly at low carrier concentrations and then curve downward at higher values. As the percent mismatch of the dopant increases, so too does the deviation from the uncorrected model. This reflects the change in aliovalent substitution efficiency with decreasing dopant ionic radius. The

mean free path of the free carriers is reduced as a larger percentage of the dopant ions are incorporated interstitially, which causes the carrier mobility to decrease and  $m^*$  to increase. Even at carrier densities as high as  $1 \times 10^{21}$  cm<sup>-3</sup>, the LSPR for MZO NCs is still limited to the MIR region due to this ineffective aliovalent incorporation and its resulting effects on free carrier generation and the mobility of free carriers.

In addition to the uncorrected Drude model, the value for  $\alpha$  determined via full band structure calculations for ZnO (1.52 eV) is also plotted. <sup>57</sup> The deviation for all three MZO samples from the theoretical value for n-type ZnO reflects the number of pinned carriers that exist from various defect sites such as F-centers and the existence of a surface depletion region. The difference between the calculated values of  $\alpha$  for each sample and the literature value of 1.52 eV reflects the change in the number of pinned carriers generated depending on the dopant identity. These values (AZO-1.49 eV, GZO-1.48 eV, IZO-1.32 eV) indicate that better size matching of the dopant ion also leads to less pinned carriers being generated and ultimately higher dopant activation. The nature of these defects, surface depletion region, and the local chemical environment of dopant and host lattice nuclei is under further investigation.

# CONCLUSIONS

Al-, Ga-, and In-doped (12%), 10 nm ZnO NCs have been synthesized and observed to exhibit dopant dependent plasmonic properties. ICP-MS and spectroscopic measurements confirm dopant incorporation and free carrier generation. pXRD and TEM data show that all samples are of the wurtzite phase and that dopant incorporation has no significant effect on the size or morphology of the NCs. Analysis of the (110) reflection revealed a shift to lower values of  $2\theta$ , indicating that the smaller dopant ions (Al<sup>3+</sup>, Ga<sup>3+</sup>) incorporate interstitially as well as substitutionally. This effect results in a difference in the number of free carriers generated per dopant ion, which is confirmed via Drude fitting of the LSPR and by chemical titration. Carrier density and LSPR dampening increase inversely with M3+/Zn2+ size mismatch, which is explained by aliovalent substitution efficiency and increased el-el scattering. Interstitial dopants sit in octahedral coordination environments and likely form an insulating spinel phase (AB<sub>2</sub>X<sub>4</sub>), which lowers dopant activation. Deviations between the Drude and NOBF<sub>4</sub> calculated carrier densities indicate that there are many pinned carriers that also do not contribute to the observed LSPR. Such pinned carriers are analyzed using an advanced effective mass model, which takes into account the full band structure of ZnO and its resulting effect on  $m^*$ . These results inform on the mechanisms behind the formation of LSPRs in ZnO and are crucial for the future rational design and application of PSNCs.

# ■ ASSOCIATED CONTENT

# Supporting Information

The Supporting Information is available free of charge at https://pubs.acs.org/doi/10.1021/acs.jpcc.1c00529.

TEM, elemental analysis, and Scherrer/Vegard analysis of MZO NCs. UV-vis-NIR, FTIR spectra, and Tauc plots of MZO NCs. NOBF<sub>4</sub> titration data, photograph of samples, Drude fitted dampening constants as a function of carrier density, <sup>19</sup>F NMR of NOBF<sub>4</sub> in MeCN, and detailed surface depletion width calculations (PDF)

#### AUTHOR INFORMATION

# **Corresponding Author**

Geoffrey F. Strouse — Department of Chemistry & Biochemistry, Florida State University, Tallahassee, Florida 32306, United States; orcid.org/0000-0003-0841-282X; Email: gstrouse@fsu.edu

#### **Authors**

Carl R. Conti, III – Department of Chemistry & Biochemistry, Florida State University, Tallahassee, Florida 32306, United States; orcid.org/0000-0001-6223-6025

James R. McBride – Vanderbilt Institute of Nanoscale Science and Engineering, Nashville, Tennessee 37235, United States; Department of Chemistry, Vanderbilt University, Nashville, Tennessee 37235, United States; orcid.org/0000-0003-0161-7283

Complete contact information is available at: https://pubs.acs.org/10.1021/acs.jpcc.1c00529

### **Author Contributions**

All synthesis and characterization of the NCs was performed by C.R.C. TEM measurements were performed by J.R.M. The manuscript was prepared by C.R.C. and G.F.S.

#### **Notes**

The authors declare no competing financial interest.

#### ACKNOWLEDGMENTS

G.F.S. wishes to thank the National Science Foundation (DMR-1905757) "Tuning Plasmonic and Magneto-Plasmonic Behavior in 4-d Transition Metal Doped Indium Oxide" for funding. A portion of the transmission electron microscopy research was conducted at the Vanderbilt Institute of Nanoscale Science and Engineering.

# REFERENCES

- (1) Agrawal, A.; Cho, S. H.; Zandi, O.; Ghosh, S.; Johns, R. W.; Milliron, D. J. Localized Surface Plasmon Resonance in Semi-conductor Nanocrystals. *Chem. Rev.* **2018**, *118* (6), 3121–3207.
- (2) Liu, Z.; Zhong, Y.; Shafei, I.; Borman, R.; Jeong, S.; Chen, J.; Losovyj, Y.; Gao, X.; Li, N.; Du, Y.; et al. Tuning Infrared Plasmon Resonances in Doped Metal-Oxide Nanocrystals through Cation-Exchange Reactions. *Nat. Commun.* **2019**, *10* (1), 1394.
- (3) Yin, H.; Kuwahara, Y.; Mori, K.; Louis, C.; Yamashita, H. Properties, Fabrication and Applications of Plasmonic Semiconductor Nanocrystals. *Catal. Sci. Technol.* **2020**, *10* (13), 4141–4163.
- (4) Law, S.; Yu, L.; Rosenberg, A.; Wasserman, D. All-Semiconductor Plasmonic Nanoantennas for Infrared Sensing. *Nano Lett.* **2013**, *13* (9), 4569–4574.
- (5) Stewart, M. E.; Anderton, C. R.; Thompson, L. B.; Maria, J.; Gray, S. K.; Rogers, J. A.; Nuzzo, R. G. Nanostructured Plasmonic Sensors. *Chem. Rev.* **2008**, *108* (2), 494–521.
- (6) Elsayed, M. Y.; Ismail, Y.; Swillam, M. A. Semiconductor Plasmonic Gas Sensor Using On-Chip Infrared Spectroscopy. *Appl. Phys. A: Mater. Sci. Process.* **2017**, *123* (1), 113.
- (7) Runnerstrom, E. L.; Llordés, A.; Lounis, S. D.; Milliron, D. J. Nanostructured Electrochromic Smart Windows: Traditional Materials and NIR-Selective Plasmonic Nanocrystals. *Chem. Commun.* **2014**, 50 (73), 10555–10572.
- (8) Garcia, G.; Buonsanti, R.; Llordés, A.; Runnerstrom, E.; Bergerud, A.; Milliron, D. Near-Infrared Spectrally Selective Plasmonic Electrochromic Thin Films. *Adv. Opt. Mater.* **2013**, *1*, 215. (9) Heo, S.; Cho, S. H.; Dahlman, C. J.; Agrawal, A.; Milliron, D. J. Influence of Crystalline and Shape Anisotropy on Electrochromic Modulation in Doped Semiconductor Nanocrystals. *ACS Energy Lett.* **2020**, *5* (8), 2662–2670.

- (10) Lemos de Souza, M.; Pereira dos Santos, D.; Corio, P. Localized Surface Plasmon Resonance Enhanced Photocatalysis: An Experimental and Theoretical Mechanistic Investigation. *RSC Adv.* **2018**, *8* (50), 28753–28762.
- (11) Manzi, A.; Simon, T.; Sonnleitner, C.; Doblinger, M.; Wyrwich, R.; Stern, O.; Stolarczyk, J. K.; Feldmann, J. Light-Induced Cation Exchange for Copper Sulfide Based CO<sub>2</sub> Reduction. *J. Am. Chem. Soc.* **2015**, *137* (44), 14007–14010.
- (12) Lou, Z.; Gu, Q.; Liao, Y.; Yu, S.; Xue, C. Promoting Pd-Catalyzed Suzuki Coupling Reactions through near-Infrared Plasmon Excitation of WO<sub>3-x</sub> Nanowires. *Appl. Catal., B* **2016**, *184*, 258–263.
- (13) Mendelsberg, R. J.; Garcia, G.; Milliron, D. J. Extracting Reliable Electronic Properties from Transmission Spectra of Indium Tin Oxide Thin Films and Nanocrystal Films by Careful Application of the Drude Theory. *J. Appl. Phys.* **2012**, *111* (6), 063515.
- (14) Della Gaspera, E.; Chesman, A. S. R.; van Embden, J.; Jasieniak, J. J. Non-Injection Synthesis of Doped Zinc Oxide Plasmonic Nanocrystals. *ACS Nano* **2014**, *8* (9), 9154–9163.
- (15) Wainer, P.; Kendall, O.; Lamb, A.; Barrow, S. J.; Tricoli, A.; Gomez, D. E.; van Embden, J.; Della Gaspera, E. Continuous Growth Synthesis of Zinc Oxide Nanocrystals with Tunable Size and Doping. *Chem. Mater.* **2019**, *31* (23), 9604–9613.
- (16) Kanehara, M.; Koike, H.; Yoshinaga, T.; Teranishi, T. Indium Tin Oxide Nanoparticles with Compositionally Tunable Surface Plasmon Resonance Frequencies in the Near-IR Region. *J. Am. Chem. Soc.* **2009**, *131* (49), 17736–17737.
- (17) Schimpf, A. M.; Lounis, S. D.; Runnerstrom, E. L.; Milliron, D. J.; Gamelin, D. R. Redox Chemistries and Plasmon Energies of Photodoped In<sub>2</sub>O<sub>3</sub> and Sn-Doped In<sub>2</sub>O<sub>3</sub> (ITO) Nanocrystals. *J. Am. Chem. Soc.* **2015**, *137* (1), 518–524.
- (18) Ma, K.; Zhou, N.; Yuan, M.; Li, D.; Yang, D. Tunable Surface Plasmon Resonance Frequencies of Monodisperse Indium Tin Oxide Nanoparticles by Controlling Composition, Size, and Morphology. *Nanoscale Res. Lett.* **2014**, *9* (1), 547.
- (19) Hu, W.; Guo, S.; Gaul, J. P.; Boebinger, M. G.; McDowell, M. T.; Filler, M. A. Reversible Tuning of the Surface Plasmon Resonance of Indium Tin Oxide Nanocrystals by Gas-Phase Oxidation and Reduction. *J. Phys. Chem. C* **2017**, *121* (29), 15970–15976.
- (20) Sakamoto, M.; Kawawaki, T.; Kimura, M.; Yoshinaga, T.; Vequizo, J. J. M.; Matsunaga, H.; Ranasinghe, C. S. K.; Yamakata, A.; Matsuzaki, H.; Furube, A.; Teranishi, T. Clear and Transparent Nanocrystals for Infrared-Responsive Carrier Transfer. *Nat. Commun.* **2019**, *10* (1), 406.
- (21) Buonsanti, R.; Llordes, A.; Aloni, S.; Helms, B. A.; Milliron, D. J. Tunable Infrared Absorption and Visible Transparency of Colloidal Aluminum-Doped Zinc Oxide Nanocrystals. *Nano Lett.* **2011**, *11* (11), 4706–4710.
- (22) Zhou, D.; Wang, P.; Roy, C. R.; Barnes, M. D.; Kittilstved, K. R. Direct Evidence of Surface Charges in N-Type Al-Doped ZnO. J. Phys. Chem. C 2018, 122 (32), 18596–18602.
- (23) Janotti, A.; Van de Walle, C. G. Fundamentals of Zinc Oxide as a Semiconductor. *Rep. Prog. Phys.* **2009**, 72 (12), 126501.
- (24) Liu, L.; Mei, Z.; Tang, A.; Azarov, A.; Kuznetsov, A.; Xue, Q.-K.; Du, X. Oxygen Vacancies: The Origin of *n*-Type Conductivity in ZnO. *Phys. Rev. B: Condens. Matter Mater. Phys.* **2016**, 93 (23), 235305.
- (25) Erhart, P.; Klein, A.; Albe, K. First-Principles Study of the Structure and Stability of Oxygen Defects in Zinc Oxide. *Phys. Rev. B: Condens. Matter Mater. Phys.* **2005**, 72 (8), 85213.
- (26) Langer, J.; Jimenez de Aberasturi, D.; Aizpurua, J.; Alvarez-Puebla, R. A.; Auguié, B.; Baumberg, J. J.; Bazan, G. C.; Bell, S. E. J.; Boisen, A.; Brolo, A. G.; et al. Present and Future of Surface-Enhanced Raman Scattering. *ACS Nano* **2020**, *14* (1), 28–117.
- (27) Milekhin, A. G.; Sveshnikova, L. L.; Duda, T. A.; Yeryukov, N. A.; Rodyakina, E. E.; Gutakovskii, A. K.; Batsanov, S. A.; Latyshev, A. V.; Zahn, D. R. T. Surface-Enhanced Raman Spectroscopy of Semiconductor Nanostructures. *Phys. E* **2016**, *75*, 210–222.

- (28) Boriskina, S. V.; Ghasemi, H.; Chen, G. Plasmonic Materials for Energy: From Physics to Applications. *Mater. Today* **2013**, *16* (10), 375–386.
- (29) Boriskina, S.; Tong, J.; Huang, Y.; Zhou, J.; Chiloyan, V.; Chen, G. Enhancement and Tunability of Near-Field Radiative Heat Transfer Mediated by Surface Plasmon Polaritons in Thin Plasmonic Films. *Photonics* **2015**, 2 (2), 659–683.
- (30) Ito, D.; Yokoyama, S.; Zaikova, T.; Masuko, K.; Hutchison, J. E. Synthesis of Ligand-Stabilized Metal Oxide Nanocrystals and Epitaxial Core/Shell Nanocrystals via a Lower-Temperature Esterification Process. ACS Nano 2014, 8 (1), 64–75.
- (31) Look, D. C.; Leedy, K. D.; Vines, L.; Svensson, B. G.; Zubiaga, A.; Tuomisto, F.; Doutt, D. R.; Brillson, L. J. Self-Compensation in Semiconductors: The Zn Vacancy in Ga-Doped ZnO. *Phys. Rev. B: Condens. Matter Mater. Phys.* **2011**, 84 (11), 115202.
- (32) Bragg, W. H.; Bragg, W. L. The Reflection of X-Rays by Crystals. Proc. R. Soc. London. Ser. A, Contain. Pap. a Math. Phys. Character 1913, 88 (605), 428-438.
- (33) Shannon, R. Revised Effective Ionic Radii and Systematic Studies of Interatomic Distances in Halides and Chalcogenides. *Acta Crystallogr., Sect. A: Cryst. Phys., Diffr., Theor. Gen. Crystallogr.* **1976**, 32 (5), 751–767.
- (34) Vegard, L. Die Konstitution Der Mischkristalle Und Die Raumfüllung Der Atome. Eur. Phys. J. A 1921, 5 (1), 17–26.
- (35) Brehm, J. U.; Winterer, M.; Hahn, H. Synthesis and Local Structure of Doped Nanocrystalline Zinc Oxides. *J. Appl. Phys.* **2006**, 100 (6), 64311.
- (36) Tauc, J. Optical Properties and Electronic Structure of Amorphous Ge and Si. *Mater. Res. Bull.* **1968**, 3 (1), 37–46.
- (37) Muth, J. F.; Kolbas, R. M.; Sharma, A. K.; Oktyabrsky, S.; Narayan, J. Excitonic Structure and Absorption Coefficient Measurements of ZnO Single Crystal Epitaxial Films Deposited by Pulsed Laser Deposition. J. Appl. Phys. 1999, 85 (11), 7884–7887.
- (38) Oshikiri, M.; Imanaka, Y.; Aryasetiawan, F.; Kido, G. Comparison of the Electron Effective Mass of the N-Type ZnO in the Wurtzite Structure Measured by Cyclotron Resonance and Calculated from First Principle Theory. *Phys. B* **2001**, 298 (1), 472–476
- (39) Calzolari, A.; Nardelli, M. B. Dielectric Properties and Raman Spectra of ZnO from a First Principles Finite-Differences/Finite-Fields Approach. *Sci. Rep.* **2013**, 3 (1), 2999.
- (40) Zandi, O.; Agrawal, A.; Shearer, A. B.; Reimnitz, L. C.; Dahlman, C. J.; Staller, C. M.; Milliron, D. J. Impacts of Surface Depletion on the Plasmonic Properties of Doped Semiconductor Nanocrystals. *Nat. Mater.* **2018**, *17* (8), 710–717.
- (41) Conti, C. R.; Quiroz-Delfi, G.; Schwarck, J. S.; Chen, B.; Strouse, G. F. Carrier Density, Effective Mass, and Nuclear Relaxation Pathways in Plasmonic Sn:In<sub>2</sub>O<sub>3</sub> Nanocrystals. *J. Phys. Chem. C* **2020**, 124 (0), 28220.
- (42) Mkawi, E. M.; Ibrahim, K.; Ali, M. K. M.; Farrukh, M. A.; Mohamed, A. S. The Effect of Dopant Concentration on Properties of Transparent Conducting Al-Doped ZnO Thin Films for Efficient Cu<sub>2</sub>ZnSnS<sub>4</sub> Thin-Film Solar Cells Prepared by Electrodeposition Method. *Appl. Nanosci.* **2015**, 5 (8), 993–1001.
- (43) Nakrela, A.; Benramdane, N.; Bouzidi, A.; Kebbab, Z.; Medles, M.; Mathieu, C. Site Location of Al-Dopant in ZnO Lattice by Exploiting the Structural and Optical Characterisation of ZnO:Al Thin Films. *Results Phys.* **2016**, *6*, 133–138.
- (44) Gabás, M.; Torelli, P.; Barrett, N. T.; Sacchi, M.; Ramos Barrado, J. R. Electronic Structure of Al- and Ga-Doped ZnO Films Studied by Hard X-Ray Photoelectron Spectroscopy. *APL Mater.* **2014**, 2 (1), 12112.
- (45) Kröger, F. A.; Vink, H. J.; Seitz, F.; Turnbull, D. B. T.-S. S. P. Relations between the Concentrations of Imperfections in Crystalline Solids. *Solid State Physics* **1956**, *3*, 307–435, DOI: 10.1016/S0081-1947(08)60135-6.
- (46) Zheng, W.; Singh, K.; Wang, Z.; Wright, J. T.; van Tol, J.; Dalal, N. S.; Meulenberg, R. W.; Strouse, G. F. Evidence of a ZnCr<sub>2</sub>Se<sub>4</sub>

- Spinel Inclusion at the Core of a Cr-Doped ZnSe Quantum Dot. J. Am. Chem. Soc. 2012, 134 (12), 5577-5585.
- (47) Foley, M. E.; Meulenberg, R. W.; McBride, J. R.; Strouse, G. F. Eu<sup>3+</sup>-Doped ZnB<sub>2</sub>O<sub>4</sub> (B = Al<sup>3+</sup>, Ga<sup>3+</sup>) Nanospinels: An Efficient Red Phosphor. *Chem. Mater.* **2015**, 27 (24), 8362–8374.
- (48) Hartstein, K. H.; Schimpf, A. M.; Salvador, M.; Gamelin, D. R. Cyclotron Splittings in the Plasmon Resonances of Electronically Doped Semiconductor Nanocrystals Probed by Magnetic Circular Dichroism Spectroscopy. *J. Phys. Chem. Lett.* **2017**, *8* (8), 1831–1836.
- (49) Tandon, B.; Agrawal, A.; Heo, S.; Milliron, D. J. Competition between Depletion Effects and Coupling in the Plasmon Modulation of Doped Metal Oxide Nanocrystals. *Nano Lett.* **2019**, *19* (3), 2012–2019.
- (50) Liao, Z.-M.; Zhang, H.-Z.; Zhou, Y.-B.; Xu, J.; Zhang, J.-M.; Yu, D.-P. Surface Effects on Photoluminescence of Single ZnO Nanowires. *Phys. Lett. A* **2008**, 372 (24), 4505–4509.
- (51) Crockett, B. M.; Jansons, A. W.; Koskela, K. M.; Johnson, D. W.; Hutchison, J. E. Radial Dopant Placement for Tuning Plasmonic Properties in Metal Oxide Nanocrystals. *ACS Nano* **2017**, *11* (8), 7719–7728.
- (52) Wei, W. F. F+ Center in ZnO. Phys. Rev. B 1977, 15 (4), 2250-2253.
- (53) Soriano, V.; Galland, D. Photosensitivity of the EPR Spectrum of the F+ Center in ZnO. *Phys. Status Solidi B* **1976**, 77 (2), 739–743.
- (54) Lounis, S. D.; Runnerstrom, E. L.; Llordes, A.; Milliron, D. J. Defect Chemistry and Plasmon Physics of Colloidal Metal Oxide Nanocrystals. *J. Phys. Chem. Lett.* **2014**, *5* (9), 1564–1574.
- (55) Donovan, B. F.; Sachet, E.; Maria, J.-P.; Hopkins, P. E. Interplay between Mass-Impurity and Vacancy Phonon Scattering Effects on the Thermal Conductivity of Doped Cadmium Oxide. *Appl. Phys. Lett.* **2016**, *108* (2), 21901.
- (56) Hwang, J.-H.; Edwards, D. D.; Kammler, D. R.; Mason, T. O. Point Defects and Electrical Properties of Sn-Doped In-Based Transparent Conducting Oxides. *Solid State Ionics* **2000**, *129* (1), 135–144.
- (57) Jung, J.; Pedersen, T. G. Analysis of Plasmonic Properties of Heavily Doped Semiconductors Using Full Band Structure Calculations. *J. Appl. Phys.* **2013**, *113* (11), 114904.
- (58) Liu, Z.; Beaulac, R. Nature of the Infrared Transition of Colloidal Indium Nitride Nanocrystals: Nonparabolicity Effects on the Plasmonic Behavior of Doped Semiconductor Nanomaterials. *Chem. Mater.* **2017**, 29 (17), 7507–7514.